Journal of Alloys and Compounds 969 (2023) 172300

Contents lists available at ScienceDirect

Journal of Alloys and Compounds

journal homepage: www.elsevier.com/locate/jalcom

Understanding the corrosion behaviour of Al-Mg alloy fabricated using a Laser Powder Bed Fusion (L-PBF) Additive Manufacturing (AM) process

Juan Ignacio Ahuir-Torres [a,*], Gregory J. Gibbons [b], Geoff West [b], Amit Das [c], Hiren R. Kotadia [a,b,**]

[a] School of Engineering, Liverpool John Moores University, Liverpool L3 3AF, UK
[b] WMG, University of Warwick, Coventry CV4 7AL, UK
[c] School of Engineering and Applied Sciences, Swansea University Bay Campus, Fabian Way, Swansea SA1 8EN, UK

ARTICLE INFO

Keywords:
Aluminium
Additive manufacturing
Laser powder bed fusion
Intermetallics
Corrosion
Electrochemical Impedance Spectroscopy

ABSTRACT

Metal additive manufacturing (AM) is an emerging disruptive technology capable of manufacturing complex shaped components that are difficult to manufacture through conventional methods. However, the corrosion behaviour of AM fabricated parts must be considered for safety critical applications. For this reason, we have studied the relationship between AM fabricated Scalmalloy (Al-Mg-Sc-Zr) microstructures and their corresponding corrosion behaviours. This comparison has been drawn against a comparable commercial Al-Mg alloy (5182). The corrosion resistance of the samples in salt water was assessed via various electrochemical analytics techniques. It was observed that Scalmalloy produced better corrosion resistance than 5182 Al-alloy. This can be attributed to the spontaneous formation of a passive film on refined AM microstructure and the presence of Sc and Zr, specifically when samples were fabricated with higher density (less porosity). The alloys' corrosion mechanisms were dependent on immersion time and the microstructural features of the samples.

1. Introduction

Aluminium alloys have widespread industrial usage in the areas of automotive, aerospace, military, electrical, architectural, packaging, wind and solar energy management due to their excellent processability, high specific strength, good conductivity, acceptable corrosion resistance and good wear properties [1,2]. The applicability of Al-alloys is based on their chemical composition and, subsequently, manufacturing process and microstructure evolution. The mechanical and chemical properties of Al-alloys can be modified by addition of various alloying elements such as Si for castability (for 3xx.x series), Cu and Zn for precipitation strengthening (for 2xxx and 7xxx series) and Mg for work hardenability (for 5xxx series). Currently, these wrought alloys are manufactured through rolling, extrusion; and cast alloys are manufacture through casting techniques such as high pressure die casting and sand casting. However, in the last decade, Additive Manufacturing (AM) has received significant attention in metal manufacturing [3,4] as it overcomes many inherent limitations of the conventional manufacturing processes. For example, manufacturing complex geometries that are unachievable through conventional casting and machining methods, such as, customized implants, internal channels for cooling fluids, bionic devices, load optimised lattice structures with significant weight saving while maintaining strength and structural integrity. Significant advantages are also gained through reduced manufacturing steps and much-reduced waste [5].

AM has been shown to be very successful with many alloys such as titanium (e.g. Ti-6Al-4 V) [6], nickel (Inconel 625/718) [7], and steel (e.g. 316 L) [8]; and these have found application in real-world AM applications. In comparison, exploration of AM capability of Al-alloys has been limited to the near eutectic (shorter freezing range) Al-Si alloys (e.g. AlSi7Mg, AlSi10Mg and AlSi12Mg), because of their good printability [5]. In the last five years, many researchers have attempted to print established high strength Al-alloys (2xxx, 6xxx, 7xxx) [5,9–11]. These alloys are difficult to print by laser solidification. The alternative approach uses addition of high Q -value (growth restriction factor) solute elements (e.g. Ti [12]) to generate constitutional supercooling for nucleation ahead of the solid-liquid interface. Despite all the work on AM of wrought Al-alloys, practical acceptance has only been achieved

* Corresponding author.
** Corresponding author at: School of Engineering, Liverpool John Moores University, Liverpool L3 3AF, UK.
E-mail addresses: j.i.ahuirtorres@ljmu.ac.uk (J.I. Ahuir-Torres), h.r.kotadia@ljmu.ac.uk (H.R. Kotadia).

https://doi.org/10.1016/j.jallcom.2023.172300
Received 15 March 2023; Received in revised form 20 September 2023; Accepted 23 September 2023
Available online 25 September 2023

for Al-Mg-Sc-Zr alloy (also, called Scalmalloy®) [13]. This alloy is capable of forming fine equiaxed and columnar grain structure under Laser-Powder Bed Fusion (L-PBF) AM processing conditions, and consequently, eliminates hot-cracking defects [14]. During the solidification, Al_3Zr and Al_3Sc particles form in-situ before primary-Al nucleation and act as nucleation sites for the grain formation due to low lattice misfit [5]. In addition, during the stress reliving heat treatment at 325 °C for 4 h, nano-sized Al_3(Sc, Zr) particles precipitate from the supersaturated solid solution formed under rapid solidification (cooling rates ca. 10^3–10^8 Ks^{-1}). The tensile properties of the Scalmalloy achieved ca. 500 MPa Y.S., 525 MPa UTS, with 12% elongation at ambient temperature [5].

Al-alloy microstructures produced by AM are often distinct and complex in nature. Understanding microstructure evolution under varying solidification condition is critical to improve the material properties and soundness of AM Al components. Some of the distinctive features observed in AM Al-alloy microstructure due to the rapid solidification and distinct processing conditions are [5]: (i) heterogeneous grain structure within build: the formation of columnar primary-Al grain structures along the build direction (z), whereas grains are equiaxed in the transverse (xy) plane due to directional heat transfer under a steep temperature gradient [11]; (ii) heterogeneous grain structure within the melt pool: formation of non-uniform primary-Al grain structure. For example, fine and equiaxed grains at the melt pool boundary and columnar grains towards the centre of the melt pool [14]; (iii) grain structure: grain structure is significantly affected by processing parameters such as scanning strategy, hatch style and contour [15]; (iv) compositional heterogeneity: the evaporation of volatile elements such as Zn, Mg, Li may lead to the chemical heterogeneity within the build [16]; (v) solute trapping and metastable phase: rapid solidification in AM may lead to solute supersaturation and formation of metastable phases (e.g. Al_6Mn in Al-Mn alloy) compared to the equilibrium microstructure formed under conventional solidification processing [17]; (vi) defects: formation of lack of fusion porosity due to insufficient overlap of successive melt pools; gas porosity / void due to the moisture and adsorbed gases in the powder feedstock; hot-cracking due to alloy chemistry, freezing range and solute segregation at the grain boundary; spattering and balling due to the processing condition such as scan speed; residual stress due to the repeated heating and cooling during processing. This complex microstructure makes it challenging to establish reliable and mechanism-based microstructure–property relationships in AM processed components.

Understanding the link between the processing conditions and the resulting hierarchical microstructure evolution should allow microstructural design for improved properties. Al-alloys produced with > 99% density (under optimised conditions) have shown improvement in strength and hardness due to their ultrafine microstructure [5]. However, ductility and fatigue properties may deteriorate, mainly due to the defects and surface roughness.

As with mechanical properties, corrosion properties of Al-alloys are equally important for adoption of AM components in engineering applications. Many of the Al-alloys usually suffer pitting and/or intergranular corrosion in a saline environment due to the electrochemical interaction between second phase and/or intermetallics (IMCs) with the Al matrix [18–20]. If the IMC phase is less noble than the Al matrix, it is dissolved by the environment, and the bare alloy is then exposed to an aggressive environment [21]. In the opposite case, the Al matrix around the second phase or IMC is dissolved in the environment [22] detaching the phase and exposing the bare alloy to the aggressive environment [18,23]. An approach to minimise localised corrosion, if possible, could be to refine and disperse the IMC and second phase. This can be achieved in AM Al-Alloys but only limited investigations on corrosion in AM Al-alloys have been reported. Studies have shown that the melt pool boundary regions are most susceptible to localized corrosion and corrosion propagates preferentially along the grain boundary network of interdendritic IMCs. Scalmalloy can be a solution to this problem because a refined microstructure can be achieved without hot-cracking [14,24,25] and the corrosion resistance of the alloying elements [24,26,27]. Furthermore, notable effort has been put into developing surface treatment of AM components to improve corrosion and other surface properties [28,29]. However, little is yet known about the corrosion mechanism of high strength Al-alloys fabricated by AM and its behaviour relative to its conventional processed counterpart.

The present work investigates the corrosion resistance of the L-PBF processed Scalmalloy and compares it with an existing commercial Al-Mg alloy (5182) of similar chemical composition. Advanced characterisation techniques (SEM and TEM equipped with EDS and EBSD) were used for the microstructure analyses. The corrosion characteristics and mechanisms were investigated using various electrochemical analysis techniques (Electrochemical Noise with Asymmetrical System, Potentiodynamic Polarisation Curve and Electrochemical Impedance Spectroscopy). The influence of the microstructural and chemical properties of the samples on the corrosion mechanisms and characteristics have been assessed.

2. Experimental procedure

2.1. Sample preparation

Gas atomised Al-Mg-Sc-Zr Al-alloy powder was used as primary material for specimen fabrication by L-PBF (Heraeus Additive Manufacturing GmbH, Germany). The corrosion results from the as-fabricated samples were compared with commercially manufactured automotive grade 5182 alloy (1.5 mm thick rolled sheet) in non-sensitised condition supplied by Novelis. These two alloys with similar chemical compositions were chosen to compare corrosion mechanisms with respect to microstructural features generated through different processing routes, and to investigate the role of minor alloying elements such as Sc and Zn. These elements can affect the properties of the alloy, such as strength and corrosion resistance, by influencing the microstructure and the formation of IMCs. Understanding their contribution to the corrosion resistance of Scalmalloy can provide insights for further alloy development and optimization. The measured nominal compositions of alloys are provided in Table 1.

The diameter of Al-Mg-Sc-Zr alloy powder was measured between 10 and 80 μm *(see* Supplementary Fig. S1*)*. The L-PBF process was performed in an argon atmosphere fabricating cuboidal shaped specimens ($15 \times 20 \times 10$ mm^3) using a EOSintM 280 L-PBF 3D printer (EOS GmbH, Germany). The L-PBF printing parameters used for Sample 1 (S1) and Sample 2 (S2), are listed in Table 2. The energy density (E_d) was calculated using Eq. (1) [30],

$$E_d = \frac{P}{V_s \times h_d \times d} \quad (1)$$

where P is laser power (W), V_s is the scan velocity (mm/s), h_d is the hatch distance (mm) and d is the diameter of the laser spot (μm).

2.2. Corrosion analysis

The electrochemical assessments were conducted using a potentio/galvanostat device (Interface1010E) and were controlled using Gamry Framework software, with data analysis performed using Gamry Echem Analyst software. The experiment was conducted using three electrode

Table 1
Nominal chemical composition (in wt%) of the Al-Mg-Sc-Zr and 5182 alloys used in this study.

Alloy name	Al	Mg	Sc	Zr	Mn	Si	Fe
Scalmalloy (Al-Mg-Sc-Zr)	Balance	4.28	0.7	0.35	0.55	0.2	0.2
5182 Al-alloy	Balance	4.45	-	-	0.33	0.13	0.2

Table 2
Processing parameters for the L-PBF experiments.

Parameters	Values	Parameters	Values
Laser scan velocity, V_s (mm s^{-1})	1300 (S1) and 750 (S2)	**Laser power, P (W)**	370 (S1) and 350 (S2)
Layer thickness (μm)	30	**Energy density, E_d (GJ/m^3)**	124 (S1) and 203 (S2)
Laser spot size, d (μm)	70	**Yb-fiber laser type**	400 W
Base plate temperature, T (°C)	200	**Hatch spacing, h_d (mm)**	0.1
Sample size (mm)	15 (h) × 20 (w)× 10 (b)		

cells, with a reference electrode of 3 M KCl silver/silver chloride (3 M Ag/AgCl) and a counter working electrode of a platinum wire with a diameter of 0.7 mm. The working electrodes were the samples being analysed, which included AM and 5182 Al-alloy samples. All corrosion experiments were conducted in 0.6 M NaCl solution, naturally aerated, at a temperature of 300.5 K. Prior to the experiments, the samples were polished at 1200 grit and cleaned, and the exposed area was defined using tape with a hole and epoxy resin to shield any possible crevices. The samples were also exposed to ambient air for 48 h before the electrochemical testing to allow for passive film generation on the sample surface.

The electrochemical evaluation was passive (open circuit potential and zero resistance ammeter), active with direct current (potentiodynamic polarisation curve), and alternating current (electrochemical impedance spectroscopy). The Electrochemical Noise (EN) was conducted with the Open Circuit Potential (OCP) and Zero Resistance Ammeter (ZRA) tests conducted at the same time. EN was asymmetrical system electrochemical noise (AEN) because the three-electrode cell was formed using the reference, counter and working electrodes [31]. The potential and current densities were measured for 2 h with 0.05 s acquisition time.

The Potentiodynamic Polarisation Curves (PPC) were conducted with specific conditions. The initial potential was set at the potential at open circuit − 0.3 V, and the voltage scan rate was 0.167 mVs^{-1}. The current density was limited to 10 $mAcm^{-2}$, and the reversal potential was set to 3 V vs the reference electrode potential. The final potential was set to be the same as the initial potential. The potential at open circuit was determined after immersing the samples in 0.6 M NaCl for two hours.

The Electrochemical Impedance Spectroscopy (EIS) was carried out at 5 mV root mean square (RMS) of potential amplitude, a frequency range from 0.01 Hz to 100 kHz and 10 points per frequency decade (10 points in the frequency range from 100 kHz to 10 kHz, another 10 points in the frequency range from 10 kHz to 1 kHz etc.). EIS was conducted over 4 days (at 2 h, 24 h, 48 h, 72 h and 96 h) under immersion in NaCl to evaluate the corrosion mechanism. The equivalent circuit of the EIS data were obtained through Gamry Echem Analyst software to analyse the corrosion mechanism.

To ensure the consistency of results, all electrochemical experiments were conducted at least three times, and the repeatability of the results was confirmed (see Supplementary results for repeatability). It is important to note that some details about the analysis are incorporated with the results, which will provide a clearer understanding of the findings.

2.3. Microstructural characterisation and analysis

Microstructural analysis was performed on the samples before and after the corrosion experiments (PPC). Samples were mounted in a conductive bakelite resin and ground and polished using standard metallographic procedures. For EBSD analysis a final stage vibrational polishing step using colloidal silica was performed to minimise preparation induced deformation. The microstructural analysis was conducted using a field emission gun - scanning electron microscope (Dualbeam FEG-SEM/FIB, Versa 3D) equipped with an Oxford Instruments Ultim Max 170 energy-dispersive X-ray spectroscopy (EDS) and Symmetry 2 Electron Backscatter Diffraction (EBSD) detectors. EDS was used to identify the chemistry and composition of IMCs while EBSD was used to study the grain size and grain orientation. EBSD mapping was carried at a 20 kV acceleration voltage and a step size of 0.2 μm. As built AM samples were also investigated under Scanning Transmission Electron Microscopy (S/TEM) (Talos F200X- Thermo Fisher Scientific, USA) with samples prepared using a dual-beam focused ion beam SEM (Scios- Thermo Fisher Scientific, USA). Microstructure analyses were performed using various software: quantification of porosity and powder size distribution performed using ImageJ, EDS analysis using Aztec (oxford instruments), EBSD microstructure processed through AZtecCrystal (oxford instruments). The precipitation of the grain boundary β-Al_3Mg_2 phase in the 5182 Al-alloy was analysed using H_3PO_4 etching following the ASTMB928 standard. Phase evolution calculation was performed using Thermo-Calc software (TCAL 4: Mobile v4.0 and MOBALE3: Al-Alloys Mobility v3.0 packages). The as-built samples density was measured through Archimedes' density measurement following ASTM B962 guidelines.

3. Results and discussion

3.1. Microstructural study (as fabricated and received)

The overall microstructure of L-PBF (as-fabricated) Scalmalloy processed using different L-PBF parameters, and 5182 Al-alloy (commercially manufactured) are presented in Fig. 1. The defects in L-PBF fabricated specimens varied with the laser power and scanning speed, which are expected to be the primary contributors to the build specimen density. The observed defects, including lack of fusion, gas porosity, micro-cracks, and un-melted powder (possibly caused by powder oxidation [32]), are evident in (Fig. 1 (a - i) and (b)). Sample S1, processed at a scanning speed of 1300 mm s^{-1} and laser power of 370 W (E_d =124 GJ/m^3), achieved a density of approximately 97%. By decreasing the scanning speed (S2) to 750 mm s^{-1} and laser power to 350 W (E_d = 203 GJ/m^3), the number of defects decreased (Fig. 1 (a - ii)), resulting in the overall density of the build increasing to 98.5%. This variation in density is also widely reported in numerous AM literatures [5,33], where a high laser energy density in general contributes to a higher relative density. A low energy density is insufficient for complete melting of the powder, resulting in the formation of partially molten particles and unfused area / voids. During the solidification of molten metal, gas becomes trapped, and material shrinkage leads to the formation of voids as it cools. In contrast, a suitable high energy density is conducive to a large melt pool and reduces voids leading to components with a high relative density and better mechanical properties.

The typical as-fabricated L-PBF microstructure of Scalmalloy is shown in Fig. 2 (a) and (b), revealing a microstructure consisting of a distribution of columnar and equiaxed grains. The different melt pools can be distinguished by the fine equiaxed grains distributed along the melt pool boundaries with a shell-like shape. The grain size statistics for specimen S2 are presented in Fig. 2(d). Fine grains constitute around 30% of the overall area, and the dimensions for columnar grains are from ~ 6–34 μm. Solidification initiates at the base of the melt pool and nucleated grains grow epitaxially under a high ratio of thermal gradient (G) to growth rate (Rg) in the direction opposite to the heat flux, thereby generating columnar grains [34].

To further investigate the microstructural detail and the elemental distribution in the L-PBF fabricated Scalmalloy, STEM-EDS maps (Fig. 3 (a)) were collected. These results show the presence of fine Al_3Sc particles within the equiaxed grains. According to Thermo-Calc prediction (Fig. 4), the primary Al_3Sc forms at around 700 °C before the Al solidification at 635 °C. As solidification initiates at the base of the melt pool, relatively slow initial cooling provides sufficient time for Sc diffusion to

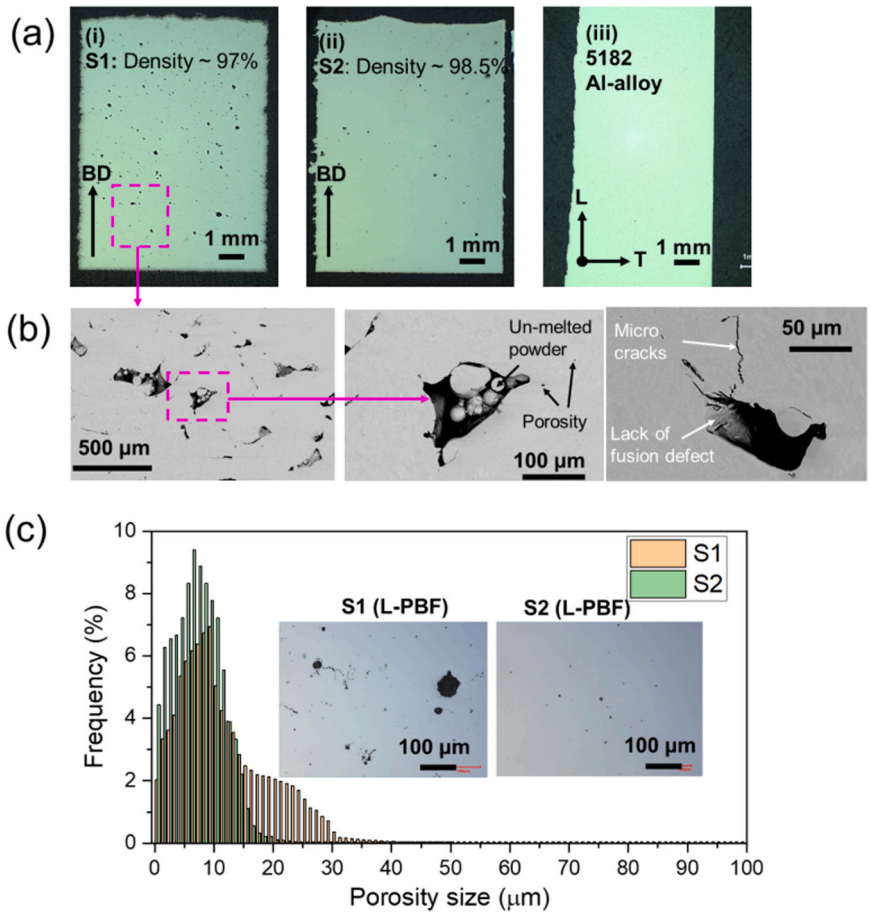

Fig. 1. (a) Optical microstructure of L-PBF (build direction, z) samples and 5182 Al-alloy (transverse – longitudinal direction) sample, (b) magnified SEM-backscattered electron (BSE) images showcase the different forms of defects in L-PBF. and (c) the statistical analysis of the porosity distribution on L-PBF samples is accompanied by inserted optical images, which reveal the porosity size and distribution comparison between sample S1 and S2. Note that density of L-PBF samples was measured through Archimedes' principle (ASTM B962).

form Al_3Sc precipitates. It is important to note that these particles have the potential to transform into $Al_3(Sc, Zr)$ if the sample undergoes slow cooling during the heat-treatment process or any thermomechanical processing [35–37]. It is also reported that Al_3Sc has better crystallographic orientation relationships (ORs) matching with Al [38]:

$$\text{OR1: } [011]_{Al} \quad \left\| [011]_{Al_3Sc} \& (\bar{2}00)_{Al} \right\| (\bar{2}00)_{Al_3Sc}$$

$$\text{OR2: } [\bar{1}12]_{Al} \quad \left\| [\bar{1}12]_{Al_3Sc} \& (\bar{1}1\bar{1})_{Al} \right\| (\bar{1}1\bar{1})_{Al_3Sc}$$

Thereby, Al_3Sc particles act as effective nucleation sites for Al grains. This is the underlying reason for the formation of fine equiaxed grains (Figs. 2(a) and 3(a)), which are found mainly at the melt pool boundaries. However, as solidification proceeds, the faster cooling and the steep thermal gradient evolving in the melt pool may prevent Al_3Sc nucleation and Sc trapping in the solidifying Al grains leading to columnar grains at the top centre of the melt pool, as shown in Fig. 2(a) and (b). This is contributed by the limited diffusion of Sc solute atoms due to the rapid increase in the solidification velocity [38]. Hence, the formation of the equiaxed-columnar microstructure is strongly related to the formation of Al_3Sc IMC and their distribution along the melt pool boundaries. It is worth mentioning that the fine-equiaxed and columnar microstructures developed through Al_3Sc assisted nucleation of Al, along with the relatively short freezing range of about 55 °C, prevents solidification cracking, despite the segregation of Mg along the grain boundaries (see Fig. 4(a)).

Fig. 2(c) and Fig. 3(b) presents the results from the as-received rolled 5182 Al-alloy for comparison. Both microstructures display randomly dispersed Fe-rich α-$Al_{15}(Fe,Mn)_3Si_2$ phase and equiaxed primary-Al grain. Dark spots in the microstructures are voids, left behind when Fe-rich phases were dislodged during the polishing process. The β-(Al_2Mg_3) phase forms in 5xxx series alloys when exposed to temperatures in the range of 50–200 °C (known as sensitisation) [21]. Detailed microstructural analysis of the grain boundaries did not show any presence of β-(Al_2Mg_3) phase as the alloy was in a non-sensitised condition (Fig. 3(c) and (d)). The β-(Al_2Mg_3) phase is known to increase the susceptibility to intergranular corrosion (IGC) and stress corrosion cracking (SCC) [39,40]. Furthermore, one should note that various phases predicted by Thermo-Calc calculation (Fig. 4 (b)) are not observed in the microstructure, suggesting that these phases either dissolve or do not form under non-equilibrium solidification.

3.2. Electrochemical analyses

Fig. 5 illustrates the results of the *passive techniques* (Asymmetrical Electrochemical Nosie (AEN) formed of Open Circuit Potential (OCP) and Zero Resistance Ammeter (ZRA)) conducted within a 0.6 M NaCl solution for a duration of two hours.

The signal fluctuation observed during the test indicated the presence of a corrosion process occurring on the samples over time. These fluctuations are typically caused by the pitting /passivation cycling process at the microscale level [41,42]. In the case of Al alloys, the primary contributing factor to the corrosion process is the presence of IMC particles within the Al matrix. For the 5182 Al-alloy and Scalmalloy

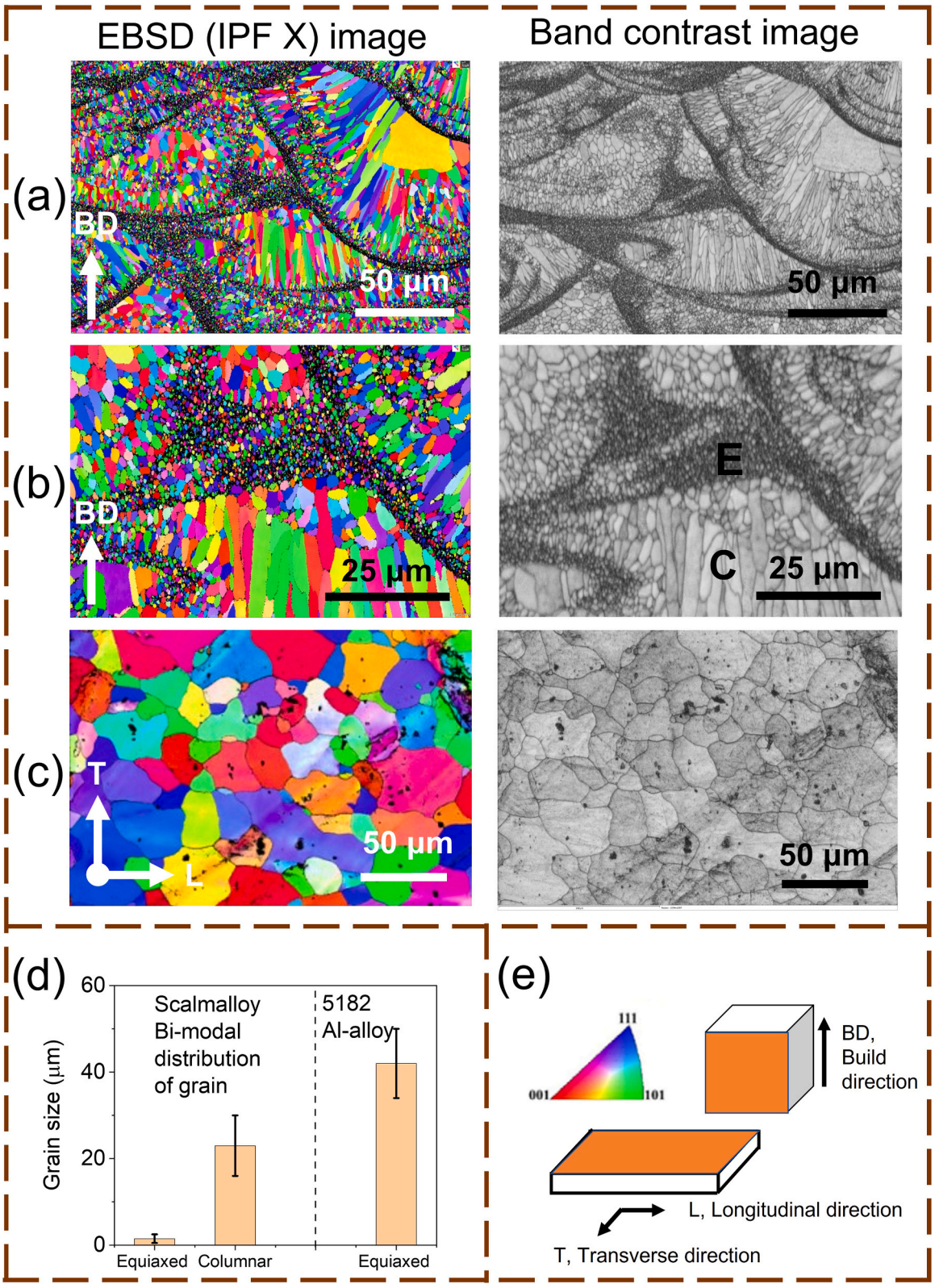

Fig. 2. EBSD derived Inverse Pole Figure (IPF) maps and band contrast image of sample microstructures: (a) and (b) L-PBF (S2) sample in the build direction (z) where (b) is at higher magnification and (c) wrought 5182 Al-alloy (transverse – longitudinal direction). (d) shows statistical analysis of grain size of the L-PBF and wrought 5182 Al-alloy samples. (e) the IPF colour triangle illustrates the colour correspondence of various orientations for EBSD images. Additionally, it includes a schematic representation of the BD (build direction for L-PBF) and T (transverse) and L (longitudinal direction) for the 5182 Al-alloy. Different grain morphologies observed are columnar (marked 'C') and equiaxed (marked 'E') in figure (b). Note that L-PBF (S1) displayed a comparable grain size to S2 (see Supplementary Fig. S2).

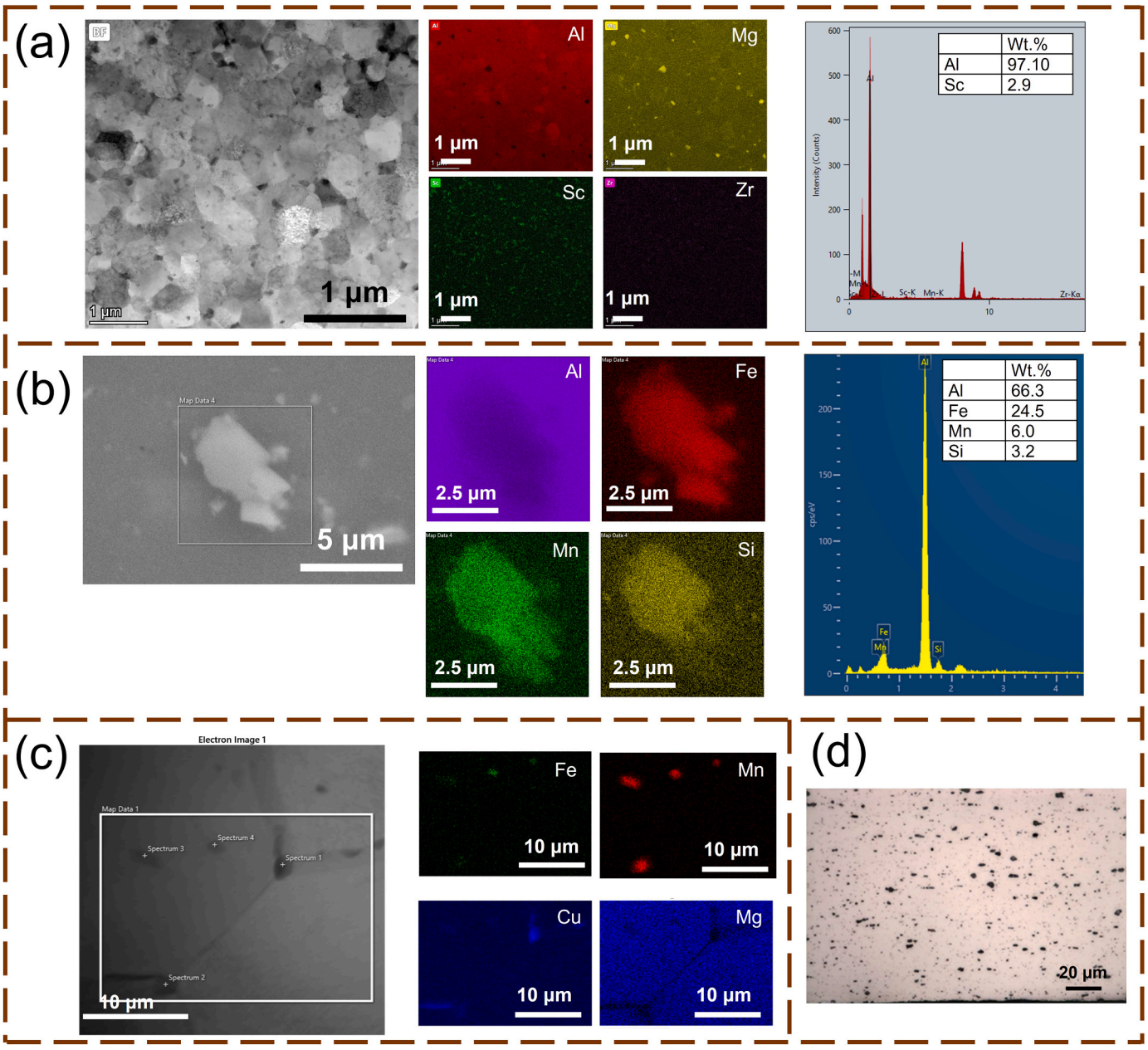

Fig. 3. (a) STEM-bright field (BF) image showing the equiaxed grain (~0.5 μm) microstructure and EDS maps with Al_3Sc precipitated phase (< 100 nm) in L-PBF fabricated Scalmalloy, and (b) SEM-secondary electron (SE) image showing an Fe-rich α-$Al_{15}(Fe,Mn)_3Si_2$ phase (range between 1 and 7 μm) and EDS maps from conventionally fabricated wrought 5182 Al-alloy. Figure (c) detailed TEM-EDS grain boundary analysis of 5182 alloys, revealing the absence of a β-Al_3Mg_2 phase. Figure (d) analysis of the same 5182 alloy using ASTMB928 standard etching, which does not exhibit clear evidence of grain boundary etching, further supporting the absence of grain boundary precipitation of the β-Al_3Mg_2 phase. Note that the dark areas in Fig. (d) represent Fe-IMCs or the voids left by detachment of such precipitates during polishing. IMCs identified using EDS data, Thermo-Calc calculation (Fig. 5) and literature.

samples used in this study, the IMC particles were α-$Al_{15}(Fe,Mn)_3Si_2$ and Al_3Sc, respectively. Both types of IMC particles act as catalytic sites for cathodic reactions, which leads to the dissolution of the particle or the surrounding matrix, and eventually leads to the initiation of pitting [43, 44].

The evolution of the OCP over time (Fig. 5**(a)**) showed more obvious changes for the 5182 Al-alloy than for L-PBF Scalmalloy samples (S1 and S2). In the 5182 Al-alloy, the OCP prominently decreased and then increased over time at dissimilar points (decreasing for ≤ 90 s, increasing from 90 to 400 s and from 1600 to 2000 s). The reduction in the OCP indicates a high chemical reactivity of the material that commonly occurs at the beginning of immersion [45]. The OCP increasing is a result of the accumulation of corrosion products (e.g., aluminium chloride, iron oxide) that decreases the chemical activity of the material by hindering the access of oxygen to the bared material [45, 46]. These events were absent for the Scalmalloy samples indicating that for these sample the chemical reaction is stable. From the ZRA measurements (Fig. 5**(b)**), sample S2 showed a current density more than two times lower than that for sample S1. The 5182 Al-alloy showed a current density in between the two L-PBF fabricated samples.

The corrosion features from the ZRA and OCP results were analysed to obtain further information about these spontaneous processes of the reduction reactions. Due to the asymmetrical nature of the electrochemical cell, these techniques only analysed the reduction reaction [31]. These features were calculated with the following Eqs. (2) – (4) and are summarised in Table 3:

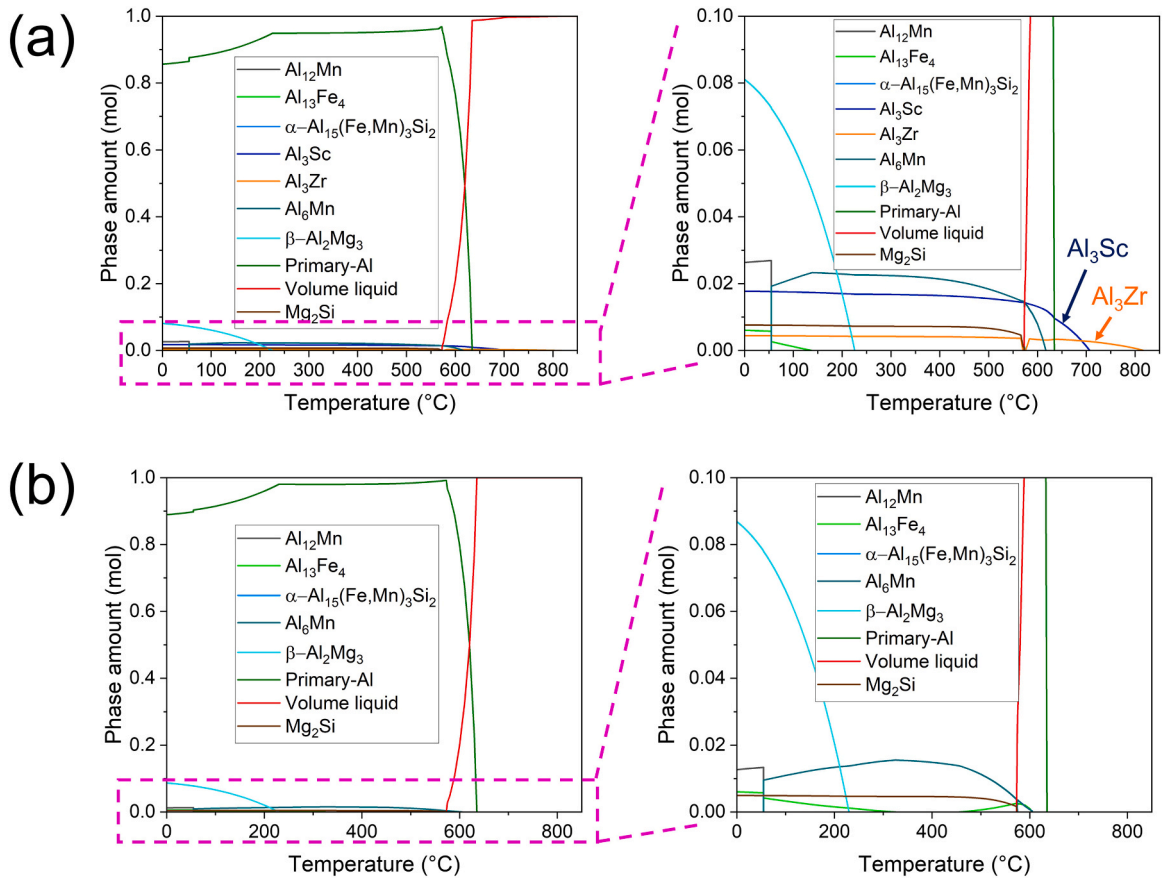

Fig. 4. Thermo-Calc generated phase evolution plots in (a) Scalmalloy and (b) wrought 5182 Al-alloy.

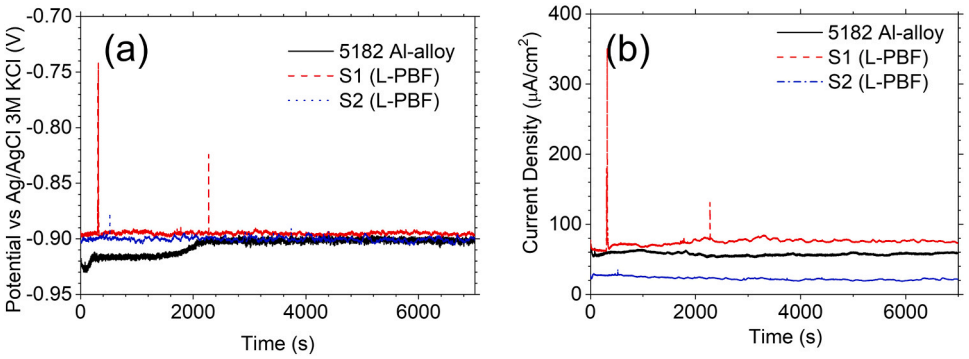

Fig. 5. (a) Evolution of the OCP and (b) current density (ZRA) over time for the 5182 Al-alloy and L-PBF built samples (S1 and S2). The repeatability of OCP and ZRA results shown in Supplementary Fig. S3 and S4.

Table 3
Calculated corrosion parameters for the 5182 Al-alloy and L-PBF fabricated Scalmalloy samples (S1 and S2).

Sample	σ_E (V)	σ_I (A/cm^2)	$I_{R.M.S.}$ (A/cm^2)	R_{EN} (Ω × cm^2)	L.I.
L-PBF S1	2.330×10^{-3}	5.841×10^{-6}	7.562×10^{-5}	400	0.078
L-PBF S2	1.827×10^{-3}	2.149×10^{-6}	2.262×10^{-5}	800	0.095
5182 Al-alloy	6.189×10^{-3}	2.160×10^{-6}	5.760×10^{-5}	3200	0.037

The current density root mean squared ($I_{R.M.S.}$) of the samples represented the kinetic of the reduction reaction. This parameter was calculated with the ZRA data using Eq. (2) [47].

$$I_{R.M.S.} = \sum_{i=N}^{N} \sqrt{\frac{I_i^2}{N}} \quad (2)$$

where, $I_{R.M.S.}$ is the root mean square current density, I_i is the current density for each measurement and N is the measurement number.

The obtained $I_{R.M.S.}$ values followed the order: S1 > 5182 Al-alloy > S2, indicating that the level of porosity has a more significant contribution to the corrosion resistance for the reduction reaction than the amount of a second phase or IMC particles during the first two hours after immersion. The high porosity in the S1 sample is more detrimental in reducing the corrosion resistance, as pores are areas where metastable pitting can be generated and are weak zones of the oxide layer [48]. The porosity can also enlarge the reaction area of the sample within an

aggressive environment, producing an increase in $I_{R.M.S.}$. The lowest $I_{R.M.S.}$ calculated in the S2 sample is presumably due to the low porosity (in comparison with the S1 sample) and the size refinement of the IMCs (in comparison with the α-$Al_{15}(Fe,Mn)_3Si_2$ of the 5182 Al-alloy). IMCs with cathodic effects act as cathodic areas where the oxygen can be reduced [49,50].

The electrochemical noise corrosion resistance (R_{EN}) was estimated through Eq. (3) [47,51] using the OCP and ZRA data:

$$R_{EN} = \frac{\sigma_E}{\sigma_I} \tag{3}$$

where, σ_E is the standard deviation of the potential values obtained using OCP and σ_I is the standard deviation of the current density values of the ZRA. The highest R_{EN} was calculated for the 5182 Al-alloy while the lowest was for the S2 sample. These results suggest that the presence of IMC and porosity can affect the corrosion resistance of the alloys differently [52]. The IMC can act as cathodic sites, leading to the initiation of pitting corrosion, while porosity can create weak zones in the oxide layer and enlarge the reaction area with the aggressive environment. The lower porosity and size refinement of IMC particles in Scalmalloy make it more corrosion-resistant compared to 5182 Al-alloy [22,31].

The local index (*L.I.*) of the samples was calculated using Eq. (4) [53,54] using ZRA data:

$$L.I = \frac{\sigma_I}{I_{R.M.S}} \tag{4}$$

Values of *L.I.* above 0.1 indicate localised corrosion, values between 0.01 and 0.1 indicate mixed localised and general corrosion, and values below 0.01 indicate general corrosion [53,54]. In this study, all three samples showed mixed corrosion.

The *direct current technique* (Potentiodynamic Polarisation Curve, PPC) results in 0.6 M NaCl for all samples are presented in Fig. 6. The overall shape of the PPC curves is different for each sample in the cathodic (reduction reactions) and anodic (oxidation reactions) branches. In 5182 Al-alloy and S1 samples, the PPC curves showed a horizontal curve at the lowest potential (−1.2 V to −1.0) in the cathodic branch due to the evolutions of the water and the oxygen dissolved in water. Within this range of potential, a part of the potential provided is utilised in the subsequent reactions [46,55]:

$$O_2 + 2H_2O + 4e^- \rightarrow 4OH^-$$

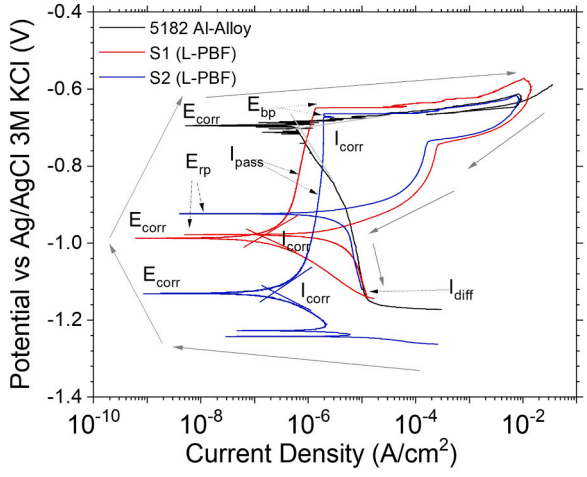

Fig. 6. Potentiodynamic Polarisation Curve (PPC) of the samples in 0.6 M NaCl. Note that the that the curve reversal occurs at the current density limit of 10 mA/cm^2 due to all tested samples having E_{bp} values lower than the reversal potential of 3 V). The repeatability of PPC results shown in Supplementary Fig. S5.

$$2H_2O + 2e^- \rightarrow 2OH^- + H_2$$

PPC of 5182 Al-alloy was characterised by a inclined vertical section in the cathodic branch that indicates mixed control (diffusion and activation) of the reduction reaction [46]. This is likely to be due to the localised distribution of the α- $Al_{15}(Fe,Mn)_3Si_2$ on the surface. This IMC phase is a cathodic area where oxygen is reduced [22] and the oxygen access to the surface is limited due to their non-uniform distribution in the Al-matrix. The anodic branch of the 5182 Al-alloy featured horizontal curves indicating activation control of the oxidation reaction and a high chemical activity in the material [46].

Scalmalloy samples showed similar PPC curves except for the water evolution that was absent in the S2 sample. The cathodic branch featured an inclined curve that indicates an activation control of the reduction reaction [56]. This is likely to be contributed to by the refinement of the primary-Al grains and Al_3Sc IMCs. The anodic branch featured a vertical curve that indicated passive control of the oxidation reaction that is consistent with the generation of a stable passive film [57–59].

The rapid solidification in L-PBF samples significantly refines the size of the Al_3Sc IMC phase and homogenises their distribution within the matrix, [24]. The presence of alloying elements Zr and Sc in Scalmalloy further enhances the production of a strong and compact passive film [44,60]. The anodic branch also included a horizontal section at high potential (around −0.650 V) due to the local degradation of the passive film. This suggests that the passive film loses its protective capacity owing to the generation of imperfections (e.g., cracks and pores) at high potentials.

Furthermore, the current density is rapidly increased owing to the cathodic area (intact and stable passive film) and is several times higher than the anodic area (bare material) [57,59]. This potential is often called the passive film breaking potential (E_{bp}). The other difference between PPCs produced from samples S1 and S2 is in the re-passivation potential (E_{rp}), which is defined as the inflexion point in the return curve. For sample S1 this potential is similar to the corrosion potential (E_{corr}), however for sample S2 the re-passivation potential is higher than E_{corr}. This indicates that the passive film in the S2 sample can be spontaneously recovered while this is not the case for the S1 sample [57]. This can be attributed to the higher porosity in the S1 sample that hinders passive film recuperation [48]. Although precipitates can influence passive film properties, these are similar in both L-PBF fabricated Scalmalloy samples and are therefore unlikely to be the cause of the observed differences. It's important to highlight that the PPC return was exclusively conducted for L-PBF fabricated samples due to the presence of a passive film observed on the PPC. The passive film is absent on the PPC for 5182 Al-alloy as the corrosion potential is the same as the passive film breaking potential ($E_{corr} = E_{pb}$). A high chemical reactivity of the passive film results in the pitting potential coinciding with the corrosion potential [61]. The main cause for the chemical activity of the passive film is the dissimilar electrochemical nature of the IMC particles in compared to that of the Al-matrix [62,63].

The PPC results, in combination with Eqs. (5–8) were used to calculate other thermodynamic and kinetic parameters for corrosion [55,58,64,65]. These can be found in Table 4. Polarisation resistance (R_p) is a kinetic corrosion feature that was estimated using Eqs. (5) to (7):

$$E_{applied} - E_{corr} = \beta_c * \ln\left(\frac{I}{I_{corr}}\right) \tag{5}$$

$$E_{applied} - E_{corr} = \beta_a * \ln\left(\frac{I}{I_{corr}}\right) \tag{6}$$

$$R_p = \frac{\beta_a * \beta_c}{2.303 * (\beta_a + \beta_c) * I_{corr}} \tag{7}$$

Table 4
List of the thermodynamic and kinetic corrosion parameters for the samples evaluated through PPC.

Parameter	Sample		
	L-PBF S1	L-PBF S2	5182 Al-alloy
β_c (V/decade)	-0.034	-0.045	-0.068
β_a (V/decade)	0.255	0.147	0.010
I_{corr} (A/cm^2)	3×10^{-7}	5×10^{-7}	9×10^{-7}
E_{corr} (V)	-0.987	-1.132	-0.695
I_p (A/cm^2)	4×10^{-7}	1×10^{-6}	-
E_{pb} (V)	-0.650	-0.664	-0.695-
ΔE_p (V)	-0.937,	-1.024,	-0.695
	-0.650	-0.664	-0.695
E_{rp} (V)	-0.939	-0.914	-
R_p ($\Omega \times$ cm^2)	50432	61288	4145
CR_{corr} (mm/Year)	0.003	0.005	0.007
CR_{pass} (mm/Year)	0.004	0.011	-
I_{diff} (A/cm^2)	-	-	1×10^{-5}
CR_{diff} (mm/Year)	-	-	0.107

where, I is the current density, $E_{applied}$ is the applied potential, I_{corr} is the corrosion current density, β_c and β_a are cathodic and anodic slopes, respectively. I_{corr} was determined by means of the intersection of the Tafel lines [58,65]. The S2 sample had higher R_p than the S1 sample, which indicates a higher corrosion resistance due to low porosity [23,48]. The lowest R_p was found for the 5182 Al-alloy because the α-$Al_{15}(Fe,Mn)_3Si_2$ phase increases the chemical activity of the passive film [62].

The kinetic parameters of the polarisation corrosion (CR_{corr}), passive (CR_{pass}) and diffusion (CR_{diff}) corrosion rates were calculated using Eq. (8) [55]:

$$CR_{corr} \quad or \quad CR_{pass} \quad or \quad CR_{diff} = \frac{(I_{corr} \quad or \quad I_{pass} \quad or \quad I_{diff} \quad) \times M}{n \times F \times d} \qquad (8)$$

Where I_{pass} is the passive film current density, I_{diff} is the diffusion current density, M is the Al molar mass (27 g/mol), n is the number of transferred electrons (3), F is Faraday's constant (96500 C/mol) and d is the density of Al (2.7 g/cm^3). In this investigation, the corrosion rates were used to provide a more visual idea of the corrosion kinetics. CR_{diff} was used to evaluate the kinetic corrosion resistance of the 5182 Al-alloy whilst CR_{pass} was employed for the Scalmalloy samples. This is because corrosion is controlled by diffusion in the 5182 Al-alloy and by the passive film in the Scalmalloy samples. CR_{diff} was higher than CR_{pass}, which showed that Scalmalloy was kinetically more corrosion resistant than the 5182 Al-alloy. The S1 sample showed lower CR_{pass} than the S2 sample, which suggests that the kinetic corrosion resistance is the lowest in the S1 sample despite its higher porosity.

Another thermodynamic parameter calculated is the passive film potential range (ΔE_p) that is defined as the potential range for the vertical section in the anodic branch. This parameter represents the potential range where the passive film is stable. The S1 sample had a lower ΔE_p than the S2 sample. This result, in combination with the possibility of passive film recovery, shows that the S2 sample was more thermodynamically corrosion resistant than the S1 samples. In the presence of pores, the homogeneity and thickness of the passive film decreased, resulting in reduced stability of the passive film [23,48]. The E_{corr} value was highest in the 5182 Al-alloy and lowest in the S2. This suggests that the 5182 Al-alloy is nobler than Scalmalloy. The E_{bp} value was mainly higher than E_{corr}. Both potentials were the same for the 5182 Al-alloy, as mentioned previously. However, the generation and stability of the passive film formed in Scalmalloy would protect the material from corrosion. This indicates that the passive films of the Scalmalloy are more thermodynamically stable than those formed on the 5182 Al-alloy.

The corrosion mechanisms at various immersion times were studied using *alternating current*, Electrochemical Impedance Spectroscopy (EIS). The Bode and Nyquist plots were used to represent the EIS data and evaluate the corrosion mechanisms using equivalent circuit methods. Two types of the Bode and Nyquist plots were observed through EIS depending on the immersion time and sample investigated, as can be seen in Fig. 7.

In the first type, the equivalent circuit (Fig. 8) for this Bode and Nyquist plot type includes four-time constants according to the EIS data. The first-time constant is represented by the horizontal curve of the Bode plot (impedance modulus vs frequency) whose equivalent circuit element is resistance (R_1). The second- and third-time constant are represented by the arc of the Nyquist plots, flat peak (θ (phase angle) vs F (frequency)) and dissimilar slopes (Z_{modul} (impendence modulus) vs F) of the Bode plots. Each time constant is formed by a constant phase element (CPE_2 and CPE_3) in a parallel circuit with a resistance (R_2 and R_3). The flat peak in the θ vs F plot indicates that processes were overlapping each other, which is represented in the equivalent circuit by placing R_2 in series with CPE_3. The fourth time constant is represented by the tails at low frequency of the Bode plots (θ vs F) and at high real impedance of the Nyquist plots, whose equivalent circuit element is the Warburg impedance (W). This element is in series with R_3 as this was observed at low frequency. The corrosion mechanisms depicted by the first type of equivalent circuit were identified in the case of the S1 sample (Fig. 7**(a)**) for 2 and 24 h of immersion, as well as for the S2 sample (Fig. 7**(b)**) and 5182 Al-alloy (Fig. 7**(c)**) before 2 h of immersion.

The second type possessed a similar equivalent circuit to the previous kind but the tails at low frequency in the Bode and at high real impedance of the Bode (θ vs F) plots were absent. The equivalent circuit was noted in the case of the S1 sample after $\geq$ 48 h of immersion (Fig. 7**(a)**), and for S2 (Fig. 7**(b)**) and 5182 Al-Alloy (Fig. 7**(c)**) after $\geq$ 24 h of immersion. The schematic diagrams for the equivalent circuits for the first and second corrosion mechanisms are shown in Fig. 8.

The size of the Nyquist plots was also altered with dissimilar evolution for each sample according to the immersion time. The spread of the Nyquist plot for the 5182 Al-alloy increased with increased immersion time at $\leq$ 48 h (Fig. 7**(c)**). These Nyquist plots at 72 h had lower spread than that for 96 h. For the L-PBF fabricated sample S1, the Nyquist plot was only increased under an immersion time between 2 and 24 h (Fig. 7**(a)**). After this immersion time, the increase in time reduced the size of the Nyquist plots. In the case of the L-PBF fabricated sample S2 (Fig. 7**(b)**), the Nyquist plot was increased with increasing immersion time. The comparative Nyquist plots of all samples are shown in Fig. 7 **(d)** for 96 h of immersion. Both 5182 Al-alloy and S2 samples show similar evolution over time with similar shape but the S1 sample had a small size.

The corrosion mechanism data were generated through the equivalent circuit simulation using *Gamry Echem Analyst* software and these are summarised in Table 5. X values calculated for the samples were between 10^{-4} and 10^{-3}, which showed an acceptable agreement between the simulation and experimental data. This good similarity between the experimental and simulation results can be seen in Fig. S11. Note that n_2 and n_3 are close to 1 indicating that CPE can be considered as capacitors [66] with a flat surface of the bared material and passive film [67].

3.3. Microstructural investigation following corrosion exposure

The microstructures showing localised corrosion attack, after PPC tests, are presented in Fig. 9 for all samples investigated. Both the top and side view of the exposed areas are presented. The localised corrosion appears to be dissimilar between the L-PBF fabricated samples and the conventionally manufactured 5182 Al-alloy sample.

In the L-PBF fabricated samples (Fig. 9(b) and (c)) corrosion is visible in the melt pool boundary where fine grains with nanoscale Al_3Sc IMCs exist (Fig. 3(a)). The microstructures perpendicular to the exposed surface confirm limited pitting, and corrosion growth predominantly in the intergranular areas around the melt pool boundary. The depth of corrosion penetration varies from 10 μm to 300 μm, depending on the location.

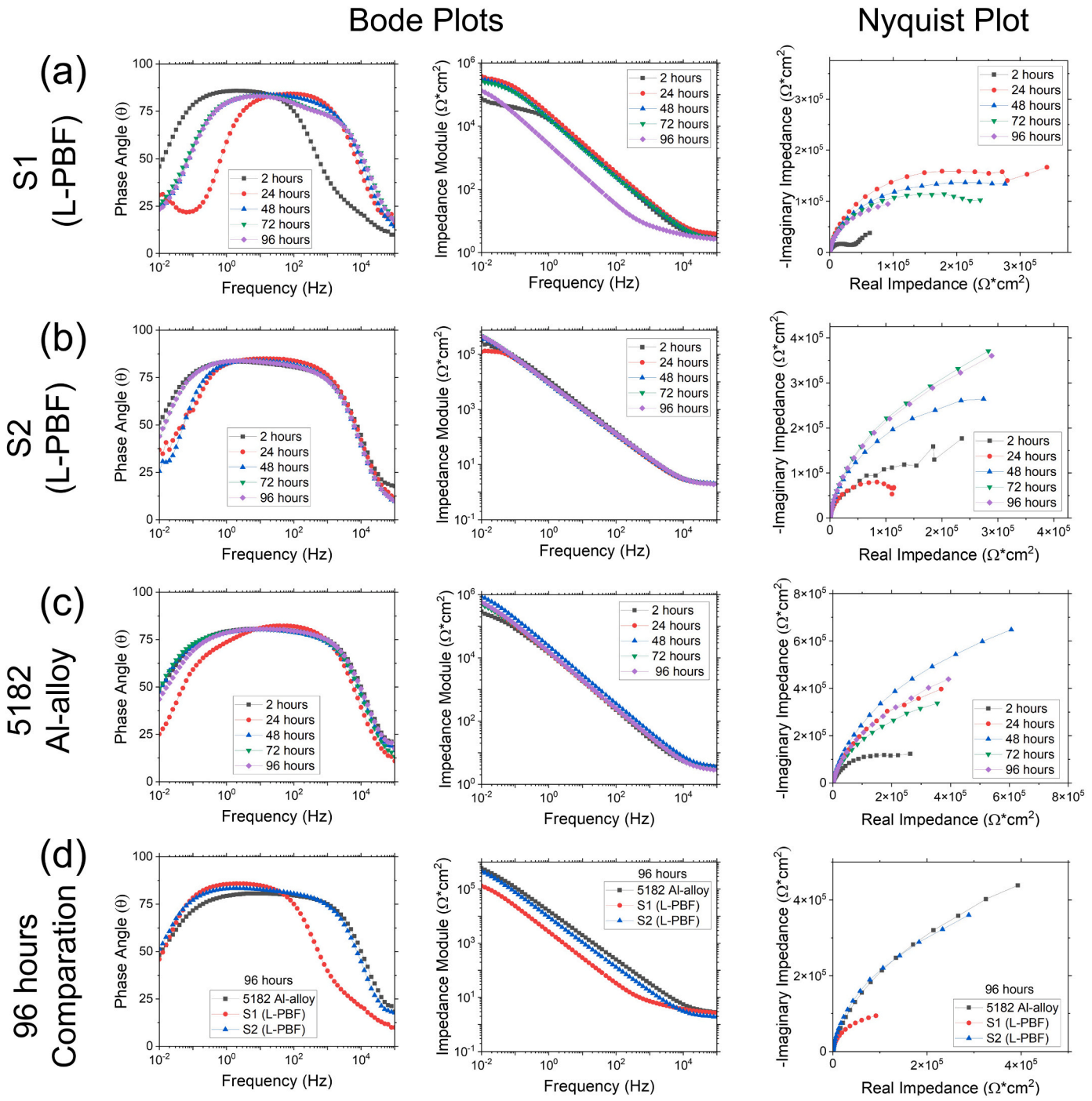

Fig. 7. Bode and Nyquist plots for the (a) and (b) L-PBF fabricated S1and S2 sample, (c) wrought 5182 Al-alloy, at 2, 24-, 48-, 72- and 96-hours immersion in 0.6 M NaCl. Additionally, (d) a comparison of the Bode and Nyquist plots for all samples at 96 h. The repeatability of Bode and Nyquist plots shown in Supplementary Fig. S6 to 10.

Fig. 9(g) to (h), from the wrought 5182 Al-alloy, confirms the presence of pitting corrosion around the Fe-rich α-$Al_{15}(Fe,Mn)_3Si_2$ IMC particles. The depth of the pits varies from 5 μm to 43 μm and are of polygonal shape in the corroded regions. The distribution of the corroded sites is more disperse compared to the L-PBF samples. High magnification SEM-BS images (Fig. 9(c), (f) and (i)) shows dissimilarity between the oxide layers in the two different samples. While the oxide layer in the 5182 Al-alloy shows visible cracks or detachment, the passive film in the L-PBF samples is relatively intact and stable without cracks or pores. Thereby, the oxide layer acts as a more resistance passive layer for the L-PBF samples.

Two microstructural features were also found to have significant impact on the electrochemical response: (i) The Fe-rich α-$Al_{15}(Fe,Mn)_3Si_2$ IMC phase observed in the 5182 Al-alloy [22] (see Fig. 3(b)) and (ii) the higher volume fraction of porosity [57] observed in the L-PBF fabricated S1 sample compared to S2 sample (see Fig. 1(a) and Supplementary Fig. S2). The oxidation products of the Scalmalloys were observed to be deeper than those of the 5182 Al-alloy; however, they appeared narrower. In contrast, the wider pitting and a higher number of sites observed in the 5182 Al-alloy resulted in a decrease in its corrosion resistance, attributed to a substantial volume of material loss. The oxidised layers of the Scalmalloys have demonstrated excellent

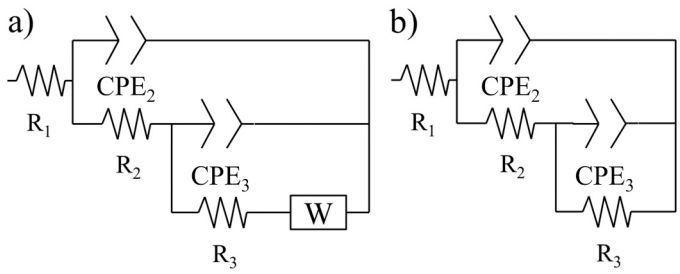

Fig. 8. Schematic drawing of the equivalent circuit for the (a) first corrosion mechanism (with Warburg impedance) and (b) second corrosion mechanism (without Warburg impedance).

protective capacity, as they appear free from cracks or pitting (see Fig. 9 (c) and Fig. 9(f)). In contrast, the passive film of the 5182 Al-alloy exhibited internal cracks, indicating a significant degradation of the passive film (see Fig. 9(i)).

3.4. Evolution of corrosion mechanisms influenced by microstructure

Through controlled experiments and detailed characterisation, it has been demonstrated that the corrosion behaviour in L-PBF fabricated samples are different from conventionally processed alloys. Alongside alloy chemistry, corrosion performance could be strongly influenced by the unique microstructure formed under rapid solidification and the presence of porosity in L-PBF samples. Findings from the electrochemical analysis were supported with microstructural observation of the size and shape of primary-Al grains, IMC size and distribution, and porosity present in the samples (Figs. 1 – 3). EBSD maps (Fig. 2) show a typical melt pool microstructure of Al-grains involving columnar growth in the centre under rapid directional solidification and fine equiaxed grains at the melt-pool boundary from enhanced Al_3Sc assisted nucleation in agreement with previous findings [14]. EDS investigation (Fig. 3) helped identify the chemical nature of the dispersed IMCs particles such as α-$Al_{15}(Fe,Mn)_3Si_2$ in wrought 5182 Al-alloy and Al_3Sc in Scalmalloy.

The electrochemical analyses of the samples indicated dissimilar corrosion features between the samples based on electrochemical analysis techniques. Firstly, the results obtained via the passive analysis of AEN showed differences with PPC data due to the passive technique being focused solely on the cathodic reaction while PPC assessment providing combined information from both the cathodic and anodic reactions [31,68]. It is observed in dissimilar values between $I_{R.M.S.}$ and I_{corr}; R_{EN} and R_p for Scalmalloy, in contrast to 5182 Al-alloy. The similarity in resistances (R_{EN} and R_p) of the 5182 Al-alloy indicates that the diffusion process velocity is similar or slower to the activation reaction rate, while noted more rapid in the S1 and S2 samples. The IMCs particles of the 5182 Al-alloys are likely to be the main cause of this slow mass transport (diffusion). The higher E_{pb} of the Scalmalloys compared with the 5182 Al-alloy indicates that the passive film of the former is more thermodynamic stable than the latter, especially for sample S2. The passive film of this sample can recover by itself due to the dense microstructure (low porosity) [57], as explained in Section 3.3. In addition, the similarity of the kinetic features (e.g., corrosion current density) indicate comparable corrosion rates for all samples.

The evolution of corrosion mechanism in the samples over time was also observed in the EIS analyses (Section 3.2). The first- and third-time constants possessed the same corrosion features for all equivalent circuits. The first time constant (R_1) is the electrical resistance of the 0.6 M NaCl [69] that remained constant over time at around 3 Ω × cm^2 (Table 6). The third process corresponds to the bare alloy chemical interaction with the environment where CPE_3, n_3 and R_3 correlates to double layer capacitance (CPE_{dl} and n_{dl}) and charge transference resistance (R_{ct}). The double layer capacitance generated through the alignment of the molecule charges. The resistance is the impedance against the electron transfer between molecules [69]. The corrosion processes for the second time constant are dissimilar based on the nature of the samples. For the 5182 Al-alloy, this time constant represents the corrosion in the pits on the passive film and therefore, CPE_2, n_2 and R_2 are called $CPE_{pitting}$, $n_{pitting}$ and $R_{pitting}$. The low value of $n_{pitting}$ (≈0.85) indicates the abrupt surface. The smooth surface shows n similar to 1 for CPE while abrupt surface possesses lower n [27]. Corrosion pit generation increases the surface roughness (Fig. 9(g-i)). These pits are produced by detachment of the α-$Al_{15}(Fe,Mn)_3Si_2$ particles on the matrix, thereby chemically activating the passive film [62,63]. This was also conformed through PPC results (E_{corr}= E_{pb}).

In the case of Scalmalloy, the second time constant represents the passive film without pits and, therefore, R_2, n_2 and CPE_2 are named as R_{pass}, n_{pass} and CPE_{pass}. This is because n_{pass} is close to 1 (≈0.95), indicating a smooth and intact passive film (without pitting). The passive film control of the PPC (E_{corr}‡ E_{bp}) analyses (Fig. 6) and SEM micrographs (Fig. 9(a-f) confirmed this association. The Scalmalloy can generate a passive film even when the corrosion potential and breaking passive film potential are different because of the absence of large α-$Al_{15}(Fe,Mn)_3Si_2$ IMC, the refined Al-grains [24] and the presence of Sc [49] and Zr solute elements [27]. A fourth time constant (W) is associated with the infinite diffusion process [70], with dissimilar origin based on the type of sample. In the case of the 5182 Al-alloy, this is due to the discrete distribution of the second phase on the surface that hinders oxygen access to the cathodic zone [22]. For the Scalmalloy, this infinite diffusion is influenced by the porosity that hinders oxygen access due to topographic reasons. Accordingly, four corrosion mechanisms were observed in the samples, as illustrated in Fig. 10.

Changes in the equivalent circuit element values with time (Table 6) indicates that the corrosion mechanism evolves over time. The reduction

Table 5
Corrosion mechanism features obtained via simulation with the equivalent circuit of the Nyquist́s and Bodés plots for the samples at various immersion times.

Sample	Time (Hours)	R_1 (Ω×cm^2)	R_2 (Ω×cm^2)	CPE_2 (μS × s^n/cm^2)	n_2	R_3 (kΩ×cm^2)	CPE_3 (μS × s^n/cm^2)	n_3	W (μS × s^n/cm^2)	X ($x10^{-3}$)
L-PBF S1	2	2.1	3	8.8	0.91	250.0	3.3	1.00	140.0	1.4
	24	3.3	18	7.0	0.94	274.0	1.0	1.00	38.0	8.2
	48	4.5	4	6.2	0.90	126.0	0.6	1.00	-	1.0
	72	3.9	17	2.0	0.98	140.0	0.5	0.97	-	1.4
	96	3.6	7	18.0	0.91	257.0	0.4	0.97	-	1.8
L-PBF S2	2	2.2	2	5.6	0.90	407.0	4.2	1.00	2.5	4.1
	24	3.5	200	1.1	0.92	285.0	0.7	1.00	-	4.1
	48	3.6	1030	1.2	0.92	1060.0	2.7	0.95	-	1.4
	72	3.5	149666	12.0	0.92	1548.2	3.6	1.00	-	1.4
	96	2.7	270000	8.6	0.92	2100.0	8.1	0.96	-	1.1
5182 Al-alloy	2	2.8	20	1.4	0.83	2582.0	3.3	1.00	59.0	1.7
	24	3.2	2	1.6	0.88	679.0	14.0	1.00	-	1.2
	48	2.9	2	2.4	0.87	111.0	11.0	0.97	-	0.4
	72	2.8	562000	1.3	0.89	395.3	34.0	0.91	-	1.1
	96	2.7	949000	1.3	0.88	126.0	67.0	1.00	-	1.2

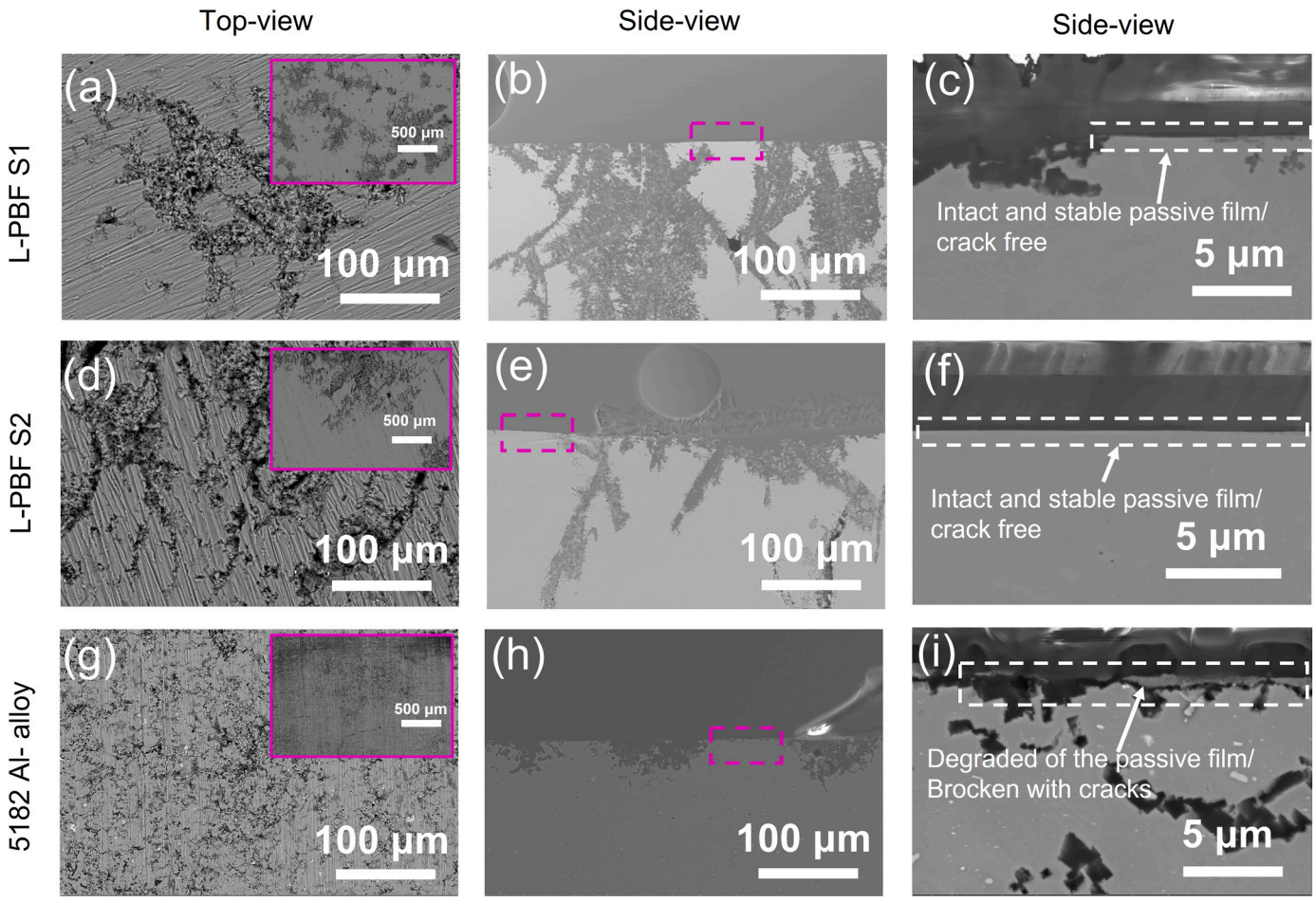

Fig. 9. Representative backscattered electron images of the corroded samples after Potentiodynamic Polarisation Curve (PPC) testing: (a) - (c) L-PBF S1 sample; (b) - (f) L-PBF S2 sample; and (g) - (i) 5182 Al-alloy sample. The top view images reveal a higher count of pitting sites in the 5182 Al-alloy compared to the L-PBF samples, with the inserted figures displaying low magnification images. However, the depth of corrosion is higher in L-PBF samples along the melt pool boundary as shown in the side-view image. Passive film in L-PBF samples is relatively intact and stable compared to broken and detached film in the 5182-alloy sample.

Table 6
The T_{pass} values for Scalmalloy according to the immersion time.

Immersion Time (hours)	CPE_{pass} (µS × s^n/cm^2)		f_{pass} (Hz)		n_{pass}		T_{pass} (nm)	
	S1	S2	S1	S2	S1	S2	S1	S2
2	8.8	5.6	200.90	79.490	0.91	0.90	1.626	2.502
24	7.0	1.1	251.00	79.490	0.94	0.92	1.672	11.247
48	6.2	1.2	12460.000	79.490	0.90	0.92	3.746	10.310
72	2.0	12	12460.000	79.490	0.98	0.92	4.714	1.0310
96	18.0	8.6	79.450	79.490	0.91	0.92	0.731	1.439

of R_{ct} and increase in CPE_{dl} with time for the 5182 Al-alloy suggests the samples were more active in the aggressive environment. The opposite evolution over time of R_{ct} was found for S2, indicating that the bare alloy is less chemically active with time. Furthermore, CPE_{dl} of S2 was similar for all immersion times. In the case of S1, these elements remained constant over time, showing that the activity of the bare material is constant over time. This indicates that the particles with dissimilar electrochemical nature to the matrix ease the activation of the 5182 Al-alloy after 2 h [22]. The refined microstructure of the Scalmalloys diminishes the chemical activity of these Al alloys [71]. The higher inactivity of S2 compared with S1 can be attributed to the higher porosity in S1 [23,48].

In the case of the 5182 Al-alloy, $R_{pitting}$ increased with time because the accumulation of the corrosion products on the pits, hinders the damage. In addition, the $CPE_{pitting}$ value remained constant with time indicating that the corrosion resistance of the 5182 Al-alloy increases over time. For Scalmalloy, the R_{pass} value remained constant and increased over time for the S1 and S2 samples, respectively. The CPE_{pass} value fluctuated over time for Scalmalloy. This indicates that the R_{pass} increase of S2 is as a result of the compaction of the passive film. The porosity of the material hinders the generation of the compacted passive film [23,48]. The thickness of the passive film (T_{pass}) is estimated using Eq. (9) and CPE_{pass} [55].

$$T_{pass} = \frac{\varepsilon_o * \varepsilon_{rAl2O3}}{CPE_{pass} * (2 * \pi * f_{pass})^{n_{pass}-1}} \quad (9)$$

where, ε_o is the permittivity of free space (8.854×10^{-14} F/cm [72]), f_{pass} is the frequency of the phase angle for passivation and ε_{rAl2O3} is the dielectric constant of alumina (8.5 [72]). Where, f_{pass} and n_{pass} are from the passive film constant time. T_{pass} values are summarised in Table 6.

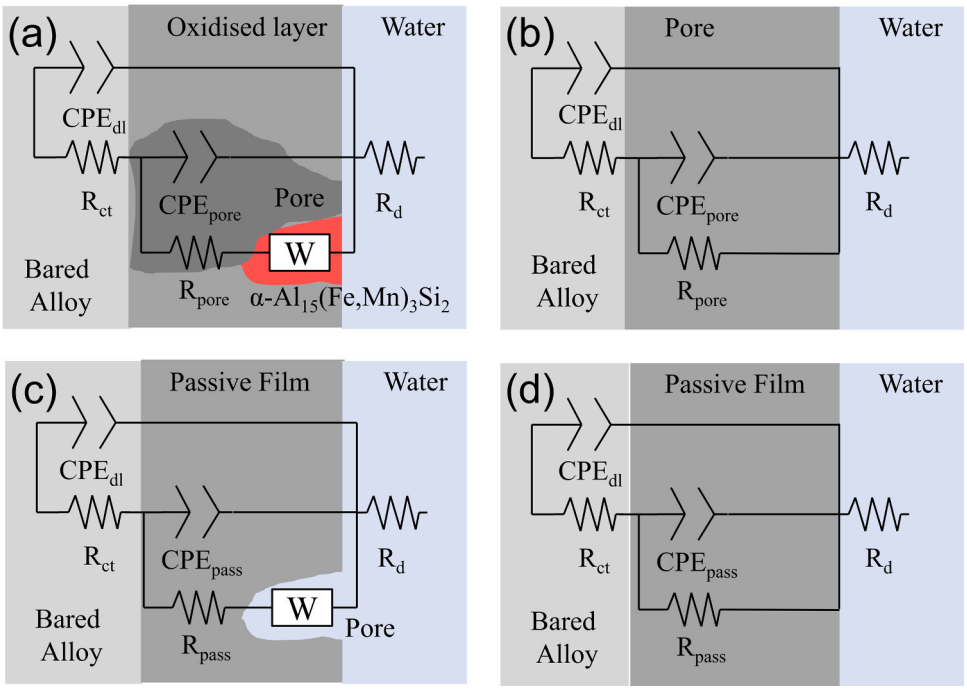

Fig. 10. Schematic drawing of the equivalent circuits (a) and (c) with and (b) and (d) without infinite diffusion process (W, four time constant). Figures (a-b) represent corrosion mechanisms for the 5182 Al-alloy while Figures (c-d) render the mechanisms for Scalmalloy.

The infinite diffusion length (L_{Diff}) was determined using W (Warburg impedance) and calculated using Eq. (10) [70]:

$$L_{Diff} = \sqrt{\frac{f_{lt}}{\sqrt{2} * W}} \tag{10}$$

where f_{lt} is the constant lifetime estimated as the maximum Bode plot phase angle at the low frequency of 0.01 Hz [70]. L_{Diff} was similar for all equivalent circuits with W, which was of the order of cm and is similar to the height of the electrochemical cell (infinite). It is worth noting that the elimination of this equivalent circuit element with immersion time is due to the microstructure features of the samples. For the 5182 Al-alloy, all second phase on the surface are detached or oxidised [67] after 24 h while for Scalmalloy, the surface oxidation smoothing the porosity on the surface because this generates a homogeneous surface [73]. This was mitigated for the S2 sample due to the lower porosity in this sample. The nature and distribution of IMC, scale of the microstructure and its refinement and the extent of porosity, therefore, were metallurgic factors significantly influencing the features and mechanisms of corrosion and their development over time. It can be noted that the elimination of W at $\geq$ 24 h for 5182 Al-alloy and S2 and, at $\geq$ 48 h for S1 can indicate that PPC of this sample could be different, which can be analysed in future work.

4. Conclusions

Despite the observation of localised corrosion from Al_3Sc IMC segregation at the grain and weld-pool boundaries, electrochemical analysis showed better corrosion resistance in L-PBF fabricated Scalmalloy compared to commercially available 5182 Al-alloy. The increased corrosion resistance in Scalmalloy and the absence of pitting, even after 24-hour immersion, is contributed by the presence of Sc and Zr helping the stability of a protective passive film on the surface of the samples inhibiting corrosion. In contrast, large $Al_{15}(Fe,Mn)_3Si_2$ IMC particles present in the 5182 Al-alloy samples acted as preferential sites for corrosion initiation leading to appreciable pitting. The corrosion performance in L-PBF Scalmalloy was further improved by low porosity and refinement of IMC particles as reduction of potential sites for corrosion initiation helped improve the integrity of the passive film. This suggests L-PBF processing parameters play a vital role in achieving desirable corrosion performance through microstructural optimisation.

CRediT authorship contribution statement

Juan Ignacio Ahuir-Torres: Conceptualization, Data curation, Investigation, Methodology, Writing - original draft. **Greg Gibbons:** Conceptualization, Funding acquisition, Methodology, Formal analysis, Writing – review & editing. **Geoff West:** Writing – review & editing. **Amit Das:** Writing – review & editing. **Hiren R. Kotadia:** Conceptualization, Resources, Funding acquisition, Formal analysis, Supervision, Writing – review & editing.

Declaration of Competing Interest

The authors declare that they have no known competing financial interests or personal relationships that could have appeared to influence the work reported in this paper.

Data availability

Data will be made available on request.

Acknowledgement

This work was partially supported by (1) Innovate UK (UK and Canada: enhancing industrial productivity): Powder Formulated Metal Additive Manufactured Actuators (PERFORMA), Grant no. 105613, (2) WMG Centre High Value Manufacturing Catapult, (3) Liverpool John Moore University, Faculty of Engineering and Technology (FET) Pump Prime Awards 2022/23.

Appendix A. Supporting information

Supplementary data associated with this article can be found in the

online version at doi:10.1016/j.jallcom.2023.172300.

References

[1] J. Davis, ASM Specialty Handbook: Aluminum and Aluminum Alloys, ASM International, Ohio, 1993, 351-316.
[2] I. Polmear, D.H. StJohn, J.F. Nie, M. Qian. Light Alloys: Metallurgy of the light metals, 5th edition.,, Butterworth-Heinemann, Oxford, 2017.
[3] T. DebRoy, H.L. Wei, J.S. Zuback, T. Mukherjee, J.W. Elmer, J.O. Milewski, A. M. Beese, A. Wilson-Heid, A. De, W. Zhang, Additive manufacturing of metallic components – Process, structure and properties, Prog. Mater. Sci. 92 (2018) 112–224.
[4] D.D. Gu, W. Meiners, K. Wissenbach, R. Poprawe, Laser additive manufacturing of metallic components: materials, processes and mechanisms, Int. Mater. Rev. 57 (2012) 133–164.
[5] H.R. Kotadia, G. Gibbons, A. Das, P.D. Howes, A review of laser powder bed fusion additive manufacturing of aluminium alloys: microstructure and properties, Addit. Manuf. 46 (2021), 102155.
[6] B. Vandenbroucke, J.P. Kruth, Selective laser melting of biocompatible metals for rapid manufacturing of medical parts, Rapid Prototyp. J. 13 (2007) 196–203.
[7] K.N. Amato, S.M. Gaytan, L.E. Murr, E. Martinez, P.W. Shindo, J. Hernandez, S. Collins, F. Medina, Microstructures and mechanical behavior of Inconel 718 fabricated by selective laser melting, Acta Mater. 60 (2012) 2229–2239.
[8] P. Bajaj, A. Hariharan, A. Kini, P. Kürnsteiner, D. Raabe, E.A. Jägle, Steels in additive manufacturing: a review of their microstructure and properties, Mater. Sci. Eng.: A 772 (2020), 138633.
[9] B.A. Fulcher, D.K. Leigh, T.J. Watt, Comparison of AlSi10Mg and Al 6061 Processed Through DMLS, Proc. 25th Solid Free. Fabr. Symp, University of Texas at Austin, (2014) 404–419.
[10] J.H. Martin, B.D. Yahata, J.M. Hundley, J.A. Mayer, T.A. Schaedler, T.M. Pollock, 3D printing of high-strength aluminium alloys, Nature 549 (2017) 365.
[11] M. Kumar, G. Gibbons, A. Das, I. Manna, D. Tanner, H.R. Kotadia, Additive manufacturing of Aluminium alloy 2024 by laser powder bed fusion: microstructural evolution, defects and mechanical properties, Rapid Prototyp. J., Rev. (2021).
[12] D. Zhang, A. Prasad, M.J. Bermingham, C.J. Todaro, M.J. Benoit, M.N. Patel, D. Qiu, D.H. StJohn, M. Qian, M.A. Easton, Grain refinement of alloys in fusion-based additive manufacturing processes, Metall. Mater. Trans. A 51 (2020) 4341–4359.
[13] K. Schmidtke, F. Palm, A. Hawkins, C. Emmelmann, Process and mechanical properties: applicability of a scandium modified al-alloy for laser additive manufacturing, Phys. Procedia 12 (2011) 369–374.
[14] A.B. Spierings, K. Dawson, M. Voegtlin, F. Palm, P.J. Uggowitzer, Microstructure and mechanical properties of as-processed scandium-modified aluminium using selective laser melting, CIRP Ann. 65 (2016) 213–216.
[15] L. Thijs, K. Kempen, J.-P. Kruth, J. Van Humbeeck, Fine-structured aluminium products with controllable texture by selective laser melting of pre-alloyed AlSi10Mg powder, Acta Mater. 61 (2013) 1809–1819.
[16] A. Mauduit, S. Pillot, H. Gransac, Study of the suitability of aluminium alloys for additive manufacturing by laser powdered fuion, U. P. B. Sci. Bull., Ser. B 79 (2017) 219–238.
[17] E.J. Lavernia, J.D. Ayers, T.S. Srivatsan, Rapid solidification processing with specific application to aluminium alloys, Int. Mater. Rev. 37 (1992) 1–44.
[18] G.M. Scamans, N. Birbilis, R.G. Buchheit, Corrosion of Aluminum and its Alloys, in: E. B.V (Ed.), Comprehensive Corrosion, Elsevier B.V, Manchester, 2010.
[19] P.R. Roberge, Corrosion engineering, McGraw-Hill Education, New York, 2008.
[20] L.L. Shrei, R.A. Jarman, G.T. Burstein, Aluminium and aluminium alloys, in: L. L. Shrei, R.A. Jarman, G.T. Burstein (Eds.), Corrosion, Metal Environment Reactions, Butterworth-Heinemann Oxford, 2000, pp. 3–38.
[21] J.A. Lyndon, R.K. Gupta, M.A. Gibson, N. Birbilis, Electrochemical behaviour of the β-phase intermetallic (Mg2Al3) as a function of pH as relevant to corrosion of aluminium–magnesium alloys, Corros. Sci. 70 (2013) 290–293.
[22] R. Ambat, A.J. Davenport, G.M. Scamans, A. Afseth, Effect of iron-containing intermetallic particles on the corrosion behaviour of aluminium, Corros. Sci. 48 (2006) 3455–3471.
[23] M. Trueba, S.P. Trasatti, Study of Al alloy corrosion in neutral NaCl by the pitting scan technique, Mater. Chem. Phys. 121 (2010) 523–533.
[24] L. Cabrera-Correa, L. González-Rovira, J. de Dios López-Castro, F.J. Botana, Pitting and intergranular corrosion of Scalmalloy® aluminium alloy additively manufactured by Selective Laser Melting (SLM), Corros. Sci. (2022), 110273.
[25] J.P. Best, X. Maeder, J. Michler, A.B. Spierings, Mechanical anisotropy investigated in the complex SLM-processed Sc-and Zr-modified Al–Mg alloy microstructure, Adv. Eng. Mater. 21 (1801113) (2019) 1801111–1801116.
[26] Y. Deng, Z. Yin, K. Zhao, J. Duan, J. Hu, Z. He, Effects of Sc and Zr microalloying additions and aging time at 120 C on the corrosion behaviour of an Al–Zn–Mg alloy, Corros. Sci. 65 (2012) 288–298.
[27] Y. Shi, Q. Pan, M. Li, X. Huang, B. Li, Effect of Sc and Zr additions on corrosion behaviour of Al–Zn–Mg–Cu alloys, J. Alloy. Compd. 612 (2014) 42–50.
[28] L. Pezzato, C. Gennari, M. Franceschi, K. Brunelli, Influence of silicon morphology on direct current plasma electrolytic oxidation process in AlSi10Mg alloy produced with laser powder bed fusion, Sci. Rep. 12 (14329) (2022) (14321-14317).
[29] E. Maleki, S. Bagherifard, M. Bandini, M. Guagliano, Surface post-treatments for metal additive manufacturing: progress, challenges, and opportunities, Addit. Manuf. 37 (2021), 101619.
[30] J. Yan, Y. Zhou, R. Gu, X. Zhang, W.-M. Quach, M. Yan, A comprehensive study of steel powders (316L, H13, P20 and 18Ni300) for their selective laser melting additive manufacturing, Metals 9 (2019) 86.
[31] D.-H. Xia, S. Song, Y. Behnamian, W. Hu, Y.F. Cheng, J.-L. Luo, F. Huet, electrochemical noise applied in corrosion science: theoretical and mathematical models towards quantitative analysis, J. Electrochem. Soc. 167 (081507) (2020) 081501–081515.
[32] X. Yang, G.J. Gibbons, D.A. Tanner, Z. Li, P. Wilson, M.A. Williams, H.R. Kotadia, Scan strategy induced microstructure and consolidation variation in the laser-powder bed fusion (L-PBF) additive manufacturing of low alloy 20MnCr5 steel, Mater. Des. 232 (2023), 112160.
[33] A.T. Sidambe, Y. Tian, P.B. Prangnell, P. Fox, Effect of processing parameters on the densification, microstructure and crystallographic texture during the laser powder bed fusion of pure tungsten, Int. J. Refract. Met. Hard Mater. 78 (2019) 254–263.
[34] J.D. Hunt, Solidification and casting of metals, The Metals Society, London, 1979, pp. 3–9.
[35] Y. Buranova, V. Kulitskiy, M. Peterlechner, A. Mogucheva, R. Kaibyshev, S. V. Divinski, G. Wilde, Al3(Sc,Zr)-based precipitates in Al–Mg alloy: effect of severe deformation, Acta Mater. 124 (2017) 210–224.
[36] O.N. Senkov, M.R. Shagiev, S.V. Senkova, D.B. Miracle, Precipitation of Al3(Sc,Zr) particles in an Al–Zn–Mg–Cu–Sc–Zr alloy during conventional solution heat treatment and its effect on tensile properties, Acta Mater. 56 (2008) 3723–3738.
[37] P. Kürnsteiner, P. Bajaj, A. Gupta, M.B. Wilms, A. Weisheit, X. Li, C. Leinenbach, B. Gault, E.A. Jägle, D. Raabe, Control of thermally stable core-shell nano-precipitates in additively manufactured Al-Sc-Zr alloys, Addit. Manuf. 32 (2020), 100910.
[38] K. Yan, Z.W. Chen, Y.N. Zhao, C.C. Ren, W.J. Lu, A.W. Aldeen, Morphological characteristics of Al3Sc particles and crystallographic orientation relationships of Al3Sc/Al interface in cast Al-Sc alloy, J. Alloy. Compd. 861 (2021), 158491.
[39] R.H. Jones, D.R. Baer, M.J. Danielson, J.S. Vetrano, Role of Mg in the stress corrosion cracking of an Al-Mg alloy, Metall. Mater. Trans. A 32 (2001) 1699–1711.
[40] R.L. Holtz, P.S. Pao, R.A. Bayles, T.M. Longazel, R. Goswami, Corrosion-fatigue behavior of aluminum alloy 5083-H131 sensitized at 448 K (175 °C), Metall. Mater. Trans. A 43 (2012) 2839–2849.
[41] A. Boag, R. Taylor, T. Muster, N. Goodman, D. McCulloch, C. Ryan, B. Rout, D. Jamieson, A. Hughes, Stable pit formation on AA2024-T3 in a NaCl environment, Corros. Sci. 52 (2010) 90–103.
[42] M.A. Amin, Metastable and stable pitting events on Al induced by chlorate and perchlorate anions—Polarization, XPS and SEM studies, Electrochim. Acta 54 (2009) 1857–1863.
[43] K. Urushino, K. Sugimoto, Stress-corrosion cracking of aged Al-Cu-Mg alloys in NaCl solution, Corros. Sci. 19 (1979) 225–236.
[44] Y. Qiu, X. Yang, J. Li, S. Xiang, J. Shi, J. Xu, R.E. Sanders, The influence of Sc and Zr additions on microstructure and corrosion behavior of AA5182 alloy sheet, Corros. Sci. 199 (2022), 110181.
[45] S.J. Kim, J.C. Park, S.K. Jang, Evaluation of Electrochemical Characteristics for Casted AC7AV Aluminum Alloy, in: Advanced Materials Research, Trans Tech Publ, 2013, pp. 54–60.
[46] K. Seong-Jong, J. Seok-Ki, H. Min-Su, P. Jae-Cheul, J.-Y. Jeong, S.-O. Chong, Mechanical and electrochemical characteristics in sea water of 5052-O aluminum alloy for ship, Trans. Nonferrous Met. Soc. China 23 (2013) 636–641.
[47] F. Mansfeld, Z. Sun, Localization index obtained from electrochemical noise analysis, Corrosion 55 (1999) 915–918.
[48] G. Sander, S. Thomas, V. Cruz, M. Jurg, N. Birbilis, X. Gao, M. Brameld, C. Hutchinson, On the corrosion and metastable pitting characteristics of 316L stainless steel produced by selective laser melting, J. Electrochem. Soc. 164 (2017) C250.
[49] N. Tuan, A. Alves, F. Toptan, A. Lopes, A. Pinto, The effect of Sc and Yb microalloying additions and aged-hardening heat treatment on corrosion behavior of Al–Mg alloys, Mater. Corros. 67 (2016) 60–71.
[50] Z. Hu, L. Wan, S. Lü, P. Zhu, S. Wu, Research on the microstructure, fatigue and corrosion behavior of permanent mold and die cast aluminum alloy, Mater. Des. 55 (2014) 353–360.
[51] R. Cottis, Interpretation of electrochemical noise data, Corrosion 57 (2001).
[52] T. Kandavel, R. Chandramouli, P. Karthikeyan, Influence of alloying elements and density on aqueous corrosion behaviour of some sintered low alloy steels, Mater. Des. 40 (2012) 336–342.
[53] E. García-Ochoa, J. González-Sánchez, F. Corvo, Z. Usagawa, L. Dzib-Pérez, A. Castañeda, Application of electrochemical noise to evaluate outdoor atmospheric corrosion of copper after relatively short exposure periods, J. Appl. Electrochem. 38 (2008) 1363–1368.
[54] R. Urzua, J. Siqueiros, L. Morales, I. Rosales, J. Uruchurtu, On-line corrosion monitoring of 70Cu 30 Ni alloy in a LiBr solution under absorption heat pump flow conditions, Port. Electrochim. Acta 27 (2009) 127–142.
[55] R.G. Kelly, J.R. Scully, D. Shoesmith, R.G. Buchheit, Electrochemical techniques in corrosion science and engineering, CRC Press, Marcel Dekker Inc, New York, 2002.
[56] E. McCaffert, Kinetics of Corrosion, in: E. McCaffert (Ed.), Introduction to Corrosion Science, Springer Science & Business Media, LLC, Alexandria, 2010, pp. 119–173.
[57] S. Anantharaj, S. Noda, M. Driess, P.W. Menezes, The pitfalls of using potentiodynamic polarization curves for tafel analysis in electrocatalytic water splitting, ACS Energy Lett. 6 (2021) 1607–1611.

[58] X. Zhang, Z.H. Jiang, Z.P. Yao, Y. Song, Z.D. Wu, Effects of scan rate on the potentiodynamic polarization curve obtained to determine the Tafel slopes and corrosion current density, Corros. Sci. 51 (2009) 581–587.
[59] J. Kruger, Passivity, in: R.W. REVIE (Ed.), UHLIG'S CORROSION HANDBOOK, ECS-The Electrochemical Society, Ontario, 2011, pp. 151–155.
[60] Z. Tang, F. Jiang, M. Long, J. Jiang, H. Liu, M. Tong, Effect of annealing temperature on microstructure, mechanical properties and corrosion behavior of Al-Mg-Mn-Sc-Zr alloy, Appl. Surf. Sci. 514 (2020), 146081.
[61] M. Smit, J. Hunter, J. Sharman, G. Scamans, J. Sykes, Effects of thermal and mechanical treatments on a titanium-based conversion coating for aluminium alloys, Corros. Sci. 46 (2004) 1713–1727.
[62] J.I. Ahuir-Torres, M. Arenas, W. Perrie, G. Dearden, J. De Damborenea, Surface texturing of aluminium alloy AA2024-T3 by picosecond laser: effect on wettability and corrosion properties, Surf. Coat. Technol. 321 (2017) 279–291.
[63] Z. Szklarska-Smialowska, Pitting corrosion of aluminum, Corros. Sci. 41 (1999) 1743–1767.
[64] G. Kear, F.C. Walsh, The characteristics of a true Tafel slope, Corros. Mater. 30 (2005) 51–55.
[65] K. Kakaei, M.D. Esrafili, A. Ehsani, Graphene and anticorrosive properties, in: Interface science and technology, Elsevier, 2019, pp. 303–337.
[66] H.W.X.Z. Yuan, C. Song, J. Zhang, EIS Equivalent Circuits, in: H.W.X.Z. Yuan, C. Song, J. Zhang (Eds.), Electrochemical Impedance Spectroscopy in PEM Fuel Cells, Springer, London, 2010, pp. 139–191.
[67] Y. Li, J. Cai, L. Guan, G. Wang, pH-dependent electrochemical behaviour of Al3Mg2 in NaCl solution, Appl. Surf. Sci. 467 (2019) 619–633.
[68] S. Esmailzadeh, M. Aliofkhazraei, H. Sarlak, Interpretation of cyclic potentiodynamic polarization test results for study of corrosion behavior of metals: a review, Prot. Met. Phys. Chem. Surf. 54 (2018) 976–989.
[69] E. McCafferty, AC Impedance, in: E. McCafferty (Ed.), Introduction to Corrosion Science, Springer, New York, 2010, pp. 427–455.
[70] T.Q. Nguyen, C. Breitkopf, Determination of diffusion coefficients using impedance spectroscopy data, J. Electrochem. Soc. 165 (2018), E826.
[71] K. Ralston, N. Birbilis, Effect of grain size on corrosion: a review, Corrosion 66 (2010), 075005-075005-075013.
[72] H.-J. Oh, K.-W. Jang, C.-S. Chi, Impedance characteristics of oxide layers on aluminium, Bull. Korean Chem. Soc. 20 (1999) 1340–1344.
[73] H.-S. Lee, J.K. Singh, J.H. Park, Pore blocking characteristics of corrosion products formed on Aluminum coating produced by arc thermal metal spray process in 3.5 wt% NaCl solution, Constr. Build. Mater. 113 (2016) 905–916.